Ultrathin poly (vinyl alcohol)/MXene nanofilm composite membrane with facile intrusion-free construction for pervaporative separations

This is the Accepted version of the following publication

Ultrathin poly (vinyl alcohol)/MXene nanofilm composite membrane with facile intrusion-free construction for pervaporative separations

Guang Yang[a,b], Zongli Xie[b,*], Aaron W. Thornton[b], Cara M. Doherty[b], Mingmei Ding[c], Hang Xu[c], Marlene Cran[a], Derrick Ng[b], Stephen Gray[a,*]

[a] *Institute for Sustainable Industries and Liveable Cities, Victoria University, PO Box 14428, Melbourne, Vic. 8001, Australia.*

[b] *CSIRO Manufacturing, Private Bag 10, Clayton South, Vic. 3169, Australia.*

[c] *College of Environmental Science, Hohai University, Nanjing 210098, China*

Corresponding authors:

* Email：stephen.gray@vu.edu.au;

* Email: zongli.xie@csiro.au;

Abstract

Molecular separations using synthetic membranes have been widely recognized as energy-efficient processes relative to conventional separation technologies. Rational design of the membrane structures for attainment of exceptionally permselective materials is highly beneficial in this respect. Herein, an ultrathin organic-inorganic hybrid nanofilm is formed on a hydrophobic polytetrafluoroethylene porous substrate through a facile and scalable solution casting process, thereby realizing an intrusion-free composite structure. Nanosizing $Ti_3C_2T_x$ MXene and sulfosuccinic acid are incorporated as nanofiller and crosslinker to manipulate the structural rigidity and free-volume property by polymer-nanofiller interaction and polymer chain crosslinking while simultaneously rendering outstanding membrane transport property, selectivity and stability. The synthesized nanofilm composite membrane with thickness down to ≈230 nm, comparable with the lateral dimension of small-sized MXene (≈142

nm), exhibits outstanding pervaporative separation of water from various aqueous-ion or -alcohol

mixtures with high throughput that is around 5-70 times of other reported polymer-based membranes.

Transport modelling of this hybrid nanofilm suggests that ultralow-resistance permeation behavior

induced by MXene nanosheets dominates as the nanofilm thickness approaches the filler size.

Keywords: MXene, pervaporation, desalination, composite membrane, fast transport.

1. Introduction

Pervaporation (PV) is an established membrane separation process driven by partial vapor

difference via deploying vacuum or a flow of inert purge on the downstream side [1]. Hydrophilic PV

for dehydration of solvents and desalination has stimulated extensive research in recent years as it is

well suited for the selective separation of water from aqueous mixtures. Particularly, PV can exhibit

advantages in separating azeotropes and close-boiling mixtures where conventional distillation

requires additional separation steps to be able to obtain pure solvents [2-5]. For desalination

applications, compared with other membrane desalination processes such as nanofiltration (NF) and

reverse osmosis (RO), PV can exhibit higher salt rejection than NF toward monovalent ions and has

the potential to cope with hypersaline water whereas huge energy and pressure are required to

overcome the osmotic pressure in RO process [6-9]. Although there is no commercial application

currently, PV desalination using polymeric membranes (polyether amide, cellulose acetate, etc.),

inorganic membrane (graphene oxide, zeolite, etc.) and hybrid membranes (chitosan/graphene oxide,

sodium alginate/graphene oxide, etc.) has been actively investigated for fundamental developments

since 1990s [10-15]. On the other hand, the current utilization of PV for solvent dehydration in industry

is multi-stage PV or combined process with distillation [16-18]. One of the key causes impeding its

further extension to standalone application or complete substitution of conventional distillation is the lack of membranes with outstanding permeability, selectivity and stability during operation. Poly (vinyl alcohol) (PVA), mainly derived from hydrolysis of polyvinyl acetate, has been a widely applied material in PV separation technology since its composite membrane was commercially launched in 1980s [19]. Compared with the emerging counterparts such as graphene oxide (GO) based, zeolite based and metal-organic framework based membranes [20-22], PVA is still competitive at the current stage for its inexpensive price, excellent processability, facile scale-up and excellent film-forming property. However, pure PVA suffers from severe swelling and tends to lose its integrity during long-term operation [23]. Manipulation of extra- and intramolecular interactions by blending with nanoscale fillers and crosslinking of the polymer chains can lead to the formation of hybrid membranes with desired integrity and enhanced separation performance [24]. In contrast with crosslinkers such as glutaraldehyde and maleic acid, sulfonated crosslinkers including sulfosuccinic acid (SSA) and 4-sulfophthalic acid are advantageous for flux enhancement due to the existence of facilitated transport sites (sulfonic acid groups) [25-27]. While for the nanofillers, the compatibility should be strongly emphasized since dispersion of nanofillers significantly affects the physicochemical properties of the resultant nanohybrid including thermal stability, mechanical property, crystallinity, free volume property and thus the subsequent separation performance [4]. Recently, 2-dimensional (2D) $Ti_3C_2T_x$ MXene (transition metal carbides) nanosheets have been intriguing in the membrane field [28-31]. Unlike graphene oxide nanosheets, $Ti_3C_2T_x$ MXene has a five-layered atomic structure built on covalent bonding and uniformly distributed surface functional groups including -OH, -O- and -F. These intrinsic attributes endow MXene with excellent mechanical rigidity, thermostability, chemical functionality as well as good dispersibility in aqueous medium, showing great promise as nanofiller in

68 polymer-based membranes.

69   To date, state-of-the-art PV membranes have been of asymmetric thin film composite construction

70 with a dense layer attached on an underlying porous support [32]. Differing from polyamide films of

71 thickness down to several nanometers by controlled interfacial polymerization [33]. PVA is solution-

72 processable and its hybrid separating layer is commonly reported to be ≈3-20 μm thick by solution

73 casting or spin coating that features in largescale fabrication for industrial use [2, 34]. It is well known

74 that reducing the membrane thickness favors the increase of permeation flux. However, obtaining a

75 scalable and ultrathin PVA based layer while maintaining its defect-free coverage on the underneath

76 support remains technically challenging. Although massive efforts have been devoted to improving the

77 perm-selectivity, formation and transport properties of the thin layer, membrane performance is also

78 influenced by the surface properties and pore structures of the substrate [35-38]. As modeled by Henis

79 et al., intrusion of casting solution into pores exerts augmented mass transport resistance due to the

80 elongated permeation path [39]. Governed by Wenzel state contact (wetted contact), it is theoretically

81 unavoidable for aqueous polymer solution to penetrate into the hydrophilic support layer [40, 41].

82 Shrinking the pore sizes of the prevailing polysulfone (PSf), polyethersulfone (PES) and

83 polyacrylonitrile (PAN) substrates to several tens of nanometers is a common route to restrain the

84 intrusion, but that will inevitably increase the overall transport resistance [42]. By contrast,

85 hydrophobic support materials are intrinsically able to reject the penetration during membrane casting,

86 providing a potential means to forming a well-aligned layer thereon [43, 44]. In this vein, microporous

87 polytetrafluoroethylene (PTFE) is proposed as a suitable support layer owing to its excellent chemical

88 and thermal stability, hydrophobicity and high porosity. More importantly, its ultralow coefficient of

89 friction is ideal for fast transport of permeates during separation process [45].

Herein, an ultrathin, intrusion-free and highly selective PVA based hybrid nanofilm containing $Ti_3C_2T_x$ MXene and SSA crosslinkers on a microporous PTFE substrate was developed via a scalable and controlled solution casting strategy. The thickness of the PVA based nanofilm with excellent separation performance toward both desalination and alcohol dehydration could be tuned down to the range of the lateral sizes of small-sized MXene, affording ultrafast permeation through the nanofilm as indicated by a transport model. Meanwhile, the incorporation of MXene caused polymer chain rigidification, decreased crystallinity and free volume increase, exhibiting favorable physicochemical properties of polymer matrix for membrane separation.

2. Experimental

2.1. Materials

The Ti_3AlC_2 powders (≥98%, 300 mesh) were purchased from Shanghai Yuehuan Material Technology Co., Ltd. Lithium fluoride (LiF, >99.0%), poly (vinyl alcohol) (PVA) (98-99% hydrolysed, molecular weight of 160,000 g mol^{-1}), SSA (70 wt% in aqueous solution) and tert-butanol (>99.0%) were acquired from Sigma-Aldrich (USA). Hydrochloric acid (HCl, 32%), methanol (>99.5 wt%), ethanol (>99.7 wt%), iso-propanol (>99.7 wt%) and salts (argentometric, calculated on dried substance) including NaCl (≥99.5%), KCl (≥99.5%), Na_2SO_4 (≥99.5%), $CaCl_2$ (≥99.5%), $MgSO_4$ (≥99.5%) were supplied by Merck KGaA (Australia). Polypropylene (PP) supported PTFE from Membrane Solution Co., Ltd was used as substrate with mean pore size of 0.57 μm for the PTFE layer. Cellulose acetate (CA, 1.2 μm), PES (0.1 μm) and nylon (0.22 μm) membrane filters were obtained from Sterlitech (USA). Milli-Q deionized (DI) water with conductivity of 18.1 MΩ cm at 25 °C was used

110   to prepare aqueous solutions.
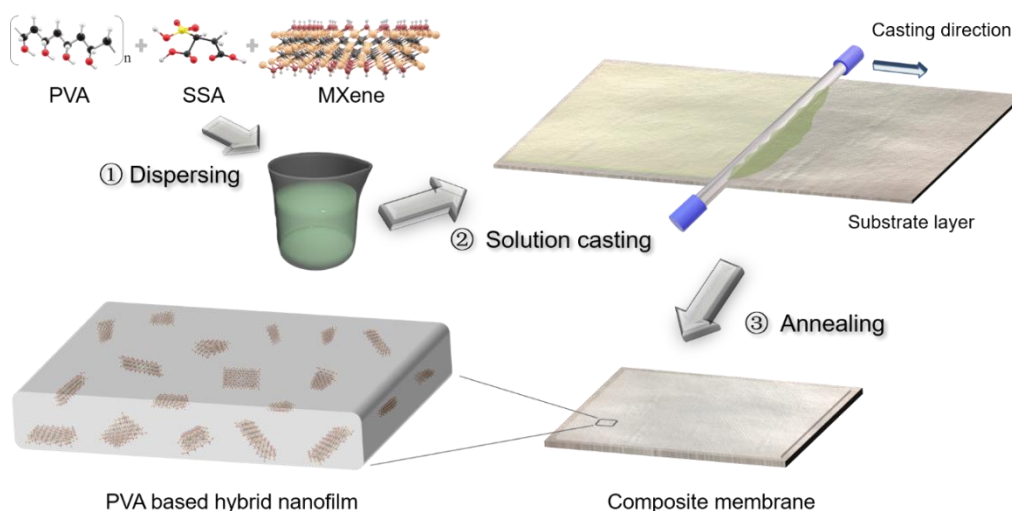
2.2. Preparation of MXene nanosheets and hybrid membranes

112    $Ti_3C_2T_x$ nanosheets were synthesized through an etching process by HCl and LiF. To be specific,

113   0.6 g of LiF was dissolved in 10 mL of 6 M HCl. After stirring for 10 min, the etching process was

114   therewith realized via adding 0.6 g of Ti_3AlC_2 powder into the abovementioned mixture and kept at

115   35 °C for 24 h with magnetic stirring. The resultant liquid mixture was diluted using DI water and

116   centrifugated repeatedly at 3500 rpm until the pH reached 6-7. The black $Ti_3C_2T_x$ sediment was then

117   collected and re-dispersed in 100 mL of DI water followed by ultrasonication in nitrogen atmosphere

118   for 3h to delaminate the MXene stacks. Lastly, the suspension was subject to centrifugation at 3500

119   rpm for 40 min and the MXene suspension was then filtrated through a nylon membrane with 0.22 μm

120   pore size. The filtrate obtained here, containing small sized MXene, was kept in a sealed reagent bottle

121   and stored in a refrigerator at 5 °C before use. The concentration of the obtained colloidal MXene

122   suspension was 5 mg mL^{-1}.

123   The dope solution was first prepared by dissolving PVA powder (1.5g) in DI water (98.5 g) at

124   90 °C to form 1.5 wt% PVA solution followed by addition of MXene and SSA dropwise. The

125   composition of the PVA/SSA/MXene mixture could be varied by changing the MXene content (1, 2

126   and 3 wt%) relative to PVA while SSA was fixed at 20 wt%. When added to the PVA solution, the

127   MXene suspension was diluted to the same volume using DI water to make PVA concentration

128   consistent in the mixture. Fig. 1 shows a schematic diagram of the fabrication process for the PVA

129   based nanofilm on the hydrophobic substrate (Fig. S1). The PVA/SSA/MXene underwent

130   ultrasonication for 20 min and was degassed (step 1) before the casting process was carried out using

a multicoater (RK PrintCoat Instruments Ltd.). It had a non-Newtonian flow property (Fig. S2) that has proven feasible for continuous liquid film casting or dip coating [46]. The membrane thickness was controlled by controlling the wet film thickness with the assistance of a casting rod of 8 μm gap (casting speed of ~0.8 cm s^{-1}) (step 2). The casting process was repeated after drying for 10 min until desired thickness was obtained. In this research, at least two casting repeats were performed. Finally, the composite membrane was treated at 85 °C in an oven for 30 min (step 3). The synthesized composite membranes were denoted as PSM/PTFE, PVA/PTFE and PS/PTFE (PVA with 20 wt% SSA and 2 wt% MXene, neat PVA and PVA with 20 wt% SSA on the PP supported PTFE substrates, respectively). Following the same method, corresponding free-standing films were also prepared for material characterization by pouring the dope on a plastic plate uniformly and peeling off once dried.

Fig. 1. Stereoscopic description of the composite membrane fabrication process. Semi-transparent arrows represent manually controlled manipulations as numbered in sequence.

2.3. Characterizations

The surface and cross-section of the composite membranes were observed by field emission scanning electron microscopy (FESEM, Zeiss Merlin Gemini 2) with the elemental composition analyzed by energy dispersive spectrum (EDS, JED-2300). The presence of functional groups was detected by attenuated total reflectance Fourier transform infrared (ATR-FTIR, Perkin-Elmer Spectrum 2000). Contact angle measurements were performed using a KSV contact angle meter (CAM200) equipped with an image capturing system. Surface charge properties were characterized by an electrokinetic analyser (SurPASS, Anton Paar). Positron annihilation lifetime spectroscopy (PALS, EG&G ORTEC fast-fast spectrometer) was deployed for the identification of the free volume properties of the membrane samples. Low field nuclear magnetic resonance (NMR, Maran Ultra 23 MHz spectrometer) were used to compare the polymer chain mobility. Differential scanning calorimetry (DSC, PerkinElmer Pyris instruments) was performed on the free-standing samples to identify the glass transition temperature (T_g) and crystalline changes. The crystalline structure of PVA and PVA based materials were assessed by X-Ray diffraction (XRD, Rigaku SmartLab X-ray diffractometer). The characteristics of $Ti_3C_2T_x$ MXene nanosheets including physicochemical properties and lateral sizes were analysed by ATR-FTIR, XRD, dynamic light scattering (DLS, Malvern Zetasizer ZS90) and transmission electron microscope (TEM, TECNAI 12 transmission electron microscope). Detailed description for each of the above measurements can be found in the supplementary information.

2.4. Pervaporation performance testing and transport modelling

PV separation tests were examined by evaluating the retention of salts or alcohol using a bench-scale stainless PV unit as described in our previous study [47]. The effective transport area of the

composite membrane was 9.6 cm^2. 0.6 M synthetic NaCl solution or other saline solutions such as KCl,

Na$_2$SO$_4$, MgCl$_2$, CaCl$_2$ and MgSO$_4$ were used as the feed solution to evaluate the desalination

performance of the PVA based composite membrane and 96 wt% C1 to C4 (methanol, ethanol, iso-

propanol and tert-butanol) alcohol-water mixture was employed to obtain the alcohol dehydration

performance. The salt solution or alcohol/water mixture was in cyclic flow on the upstream side of the

membrane with a flowrate of 50 mL min^{-1} enabled by a peristaltic pump (Masterflex). The feed

temperature was maintained at a set temperature (30, 50 or 70 °C) via a water bath. The temperature

in the feed chamber was monitored by a thermocouple (K-type). 130 Pa of vacuum pressure was

applied and kept on the permeate side by a vacuum pump for all the performance tests. The permeates

were condensed in a dry-ice (desalination) or liquid nitrogen (alcohol dehydration) cold trap. The

performance test was conducted for 3 hours after reaching a stable state whereas the stability test lasted

for 50 hours. Salt rejection (R), separation factor (α) for dehydration of alcohol and water permeation

flux (J_i) [25, 48] were employed to evaluate the separation properties of the membranes based on Eq.

(1) to (3):

$$R = \frac{C_f - C_p}{C_f} \times 100\% \tag{1}$$

$$\alpha = \frac{Y_i/Y_j}{X_i/X_j} \tag{2}$$

$$J_i = \frac{M_i}{A \times t} \tag{3}$$

For PV desalination, a pre-calibrated conductivity meter (Oakton® Con 110) was used to obtain

the salt concentrations of the feed (C_f) and permeate (C_p). For PV dehydration of alcohol, the weight

percentages of component in the feed and permeate (i and j) were referred to as X and Y, respectively.

J_i (kg m^{-2} h^{-1}) represented the permeation flux derived from the mass (M_i) of permeate collected from

187 the cold trap, the effective membrane separating area (A) and the operation time (t). The alcohol in the

188 permeate side was determined using NMR (Bruker 400 Ultrashield with Icon NMR analysis software).

189 Deviations of the characterization and performance results were obtained by testing 3 samples of the

190 same type of the composite or free-standing membrane.

191 A modified Resistance-In-Series (RIS) transport model was developed to understand the

192 mechanism of transport. The model was not considered predictive but was designed to provide insight

193 into the underlying mechanisms responsible for the observed transport phenomena. The RIS model

194 assumes that the total resistance R_{tot} throughout a hybrid is equal to the weighted sum of resistances

195 for each material, in this case the polymer R_p and the filler R_f as follows:

196 $$R_{tot} = v_f R_f + \left(1 - v_f\right)R_p$$

197 (4)

198 where v_f is the volume fraction of the filler. Resistance is equal to the inverse of permeation as:

199 $$R_{tot} = \frac{1}{J_w} = \frac{v_f}{P_f} + \frac{(1-v_f)}{P_p} \qquad\qquad (5)$$

200 where J_w represents the total water flux, P_f is the permeation through the filler and P_p is the permeation

201 through the polymer. Rearrangement of Eq.5 results in the following:

202 $$J_w = \frac{P_p P_f}{\left(P_p v_f + P_f(1-v_f)\right)} \qquad\qquad (6)$$

203 For this new hybrid material, a modification of Eq.6 is made to incorporate a percolation threshold at

204 a critical volume fraction of filler v_s. If the volume fraction of filler reaches the threshold of v_s, then a

205 percolation pathway is established and permeation through the filler becomes the dominate transport

206 pathway (i.e., $v_f = 1$). Therefore, a scaled volume fraction $v_f^* = v_f/v_s$ is incorporated into Eq.6 as follows:

$$207 \quad J_w = \frac{P_p P_f}{\left(P_p v_f^* + P_f \left(1 - v_f^*\right)\right)} \tag{7}$$

208   The relationship between the permeation flux and temperature for pervaporation generally

209   follows the Arrhenius equation (Eq. 8) where J_i is the permeate flux of the membrane, kg m^{-2} h^{-1}; F_i is

210   the pre-exponential factor; R is the gas constant (8.3145 × 10^{-3} kJ mol^{-1} K^{-1}), T is the absolute

211   temperature, K and E_a is the apparent activation energy for the permeates, kJ mol^{-1}; which relies on the

212   activation energy for diffusion as well as the sorption heat.

$$213 \quad J_i = F_i \; exp\left(-\frac{E_a}{RT}\right) \tag{8}$$

214   **3. Results and discussion**

215   *3.1. Formation of intrusion-free nanofilm composite membranes*

216   The formation of thin PVA based layer was realized upon evaporation of solvent (water) out from

217   the as-casted liquid film. During this process, the randomly dispersed MXene nanosheets were

218   immobilized in the PVA matrix as depicted in the enlarged membrane section in Fig. 1. It is noteworthy

219   to identify that the contact angle between the casting solution and PTFE was 143° (Fig. S3). This

220   follows well with the Cassie-Baxter state [41, 49], in which the porous surface exhibited a nonwetted

221   contact with liquid arising from vapor pockets trapped (air gaps) in the pores. As illustrated in Fig. 2,

222   the casting solution maintained such suspended state whereas water could evaporate via both sides of

223   the liquid film. As the water content decreased, the concentration of solid substance increased inversely,

224   resulting in narrowing of the intermolecular distance and solidifying the PVA chains to form a

225   continuous polymer matrix with dispersed MXene nanosheets and SSA, and thus the subsequent

226   nanofilm on top without pore intrusion. To further confirm this, a series of hydrophilic substrates

227 including CA, PES and nylon with various pore sizes was also coated using this casting method (Fig.

228 S4). The bottom of the thin films showed unevenly intruded geometry with those hydrophilic substrates

229 whereas a clear boundary between the film and support was present for the PTFE supported film,

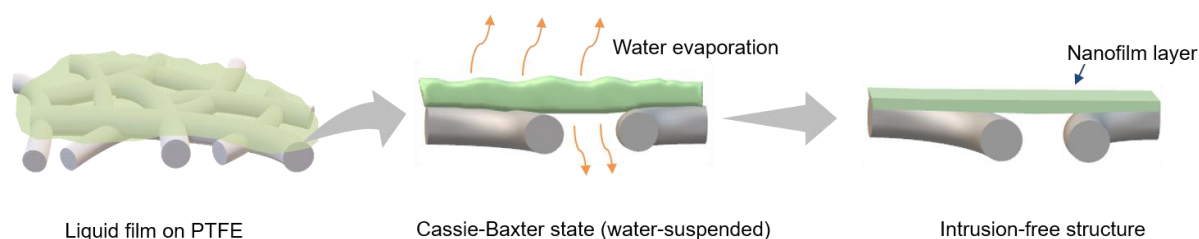230 evidencing the intrusion-free formation of PVA based layer via the abovementioned suspended state.

231

Fig. 2. Cassie-Baxter state of the casting solution on PTFE substrate layer and the following separating

233 layer formation process via water evaporation.

234   For mixed matrix membranes (MMMs), the dimensions of inorganic fillers are supposed to be

235 less than the fabricated membrane thickness so as to obtain large nanofiller-polymer interfacial area

236 while avoiding nonselective defects. In order to obtain an ultrathin separating layer, small-sized

237 $Ti_3C_2T_x$ MXene nanosheets with lateral diameters of ≈142 nm as derived from DLS measurements

238 were prepared (Fig. S5). TEM further confirmed such apparent sizes as observed in Fig. 3a and Fig.

239 S6. ATR-FTIR spectrometry and XRD (Fig. S7 and S8) identified the characteristic bands of -OH at

240 3480 cm^{-1} and C=O at 1648 cm^{-1}, as well as the (002) diffraction peak at $2\theta = 6.5°$ for the fabricated

241 MXene nanosheet stacks, in line with previous report [30]. For the fabricated PSM/PTFE (≈230 nm

242 thick active layer), the top-view morphology is presented in Fig. 3b by FESEM that exhibited a dense,

243 continuous and defect-free coverage on the underlying support. The corresponding EDS mapping of

244 the membrane surface (Fig. 3d) revealed its homogeneous elemental distributions containing C (51.7

245 wt%), O (44.2 wt%), S (3.6 wt%) and Ti (0.5 wt%). In comparison, there was no presence of S or Ti

246 for neat PVA or Ti for the PS as evidenced in Fig. S9. That demonstrated the PSM/PTFE membrane

247 had uniform dispersion of both SSA and MXene simultaneously on the surface. Meanwhile, the

248 ultrathin PSM nanofilm with thickness of ≈230 nm can be observed in the cross-section image (Fig.3c).

249 EDS line scan results (Fig. 3e) provided consistent elemental distributions with those on the nanofilm

250 surface, further affirming the successful incorporation and even dispersion state of SSA and MXene in

251 the PVA matrix. In particular, MXene nanosheets possess extensive amounts of hydrophilic groups (-

252 OH and -O-) on the surface, rendering them with excellent interfacial compatibility with PVA and thus

253 the good dispersion in the matrix. Considering thin film formation is significantly correlated to the

254 surface properties of substrate as well as the effect of nanofiller, lowering the thickness may cause

255 cracks (Fig. S10). However, the 230-nm-thick PSM did not present any obvious cracks and thus was

256 sufficiently thin to anticipate significantly improved performance. In addition, Fig. 3f presents a

257 photograph of large-area membrane (30×30 cm^2) composed of semitransparent green thin film

258 intimately laminated on the PTFE substrate with a magnified section showing its ultrathin morphology.

259 As there were no reactive groups between PVA and PFTE, the nanofilm might be interfacially adhered

260 on the substrate via interatomic and intermolecular Van der Waals forces. To investigate the stability

261 of such interfacial adhesion, the PSM/PTFE membrane was subject to long-term immersion (500 h) in

262 both water and ethanol (Fig. S11). Consequently, the membrane did not show any sign of delamination,

263 exhibiting the potential to survive in the operating environment.
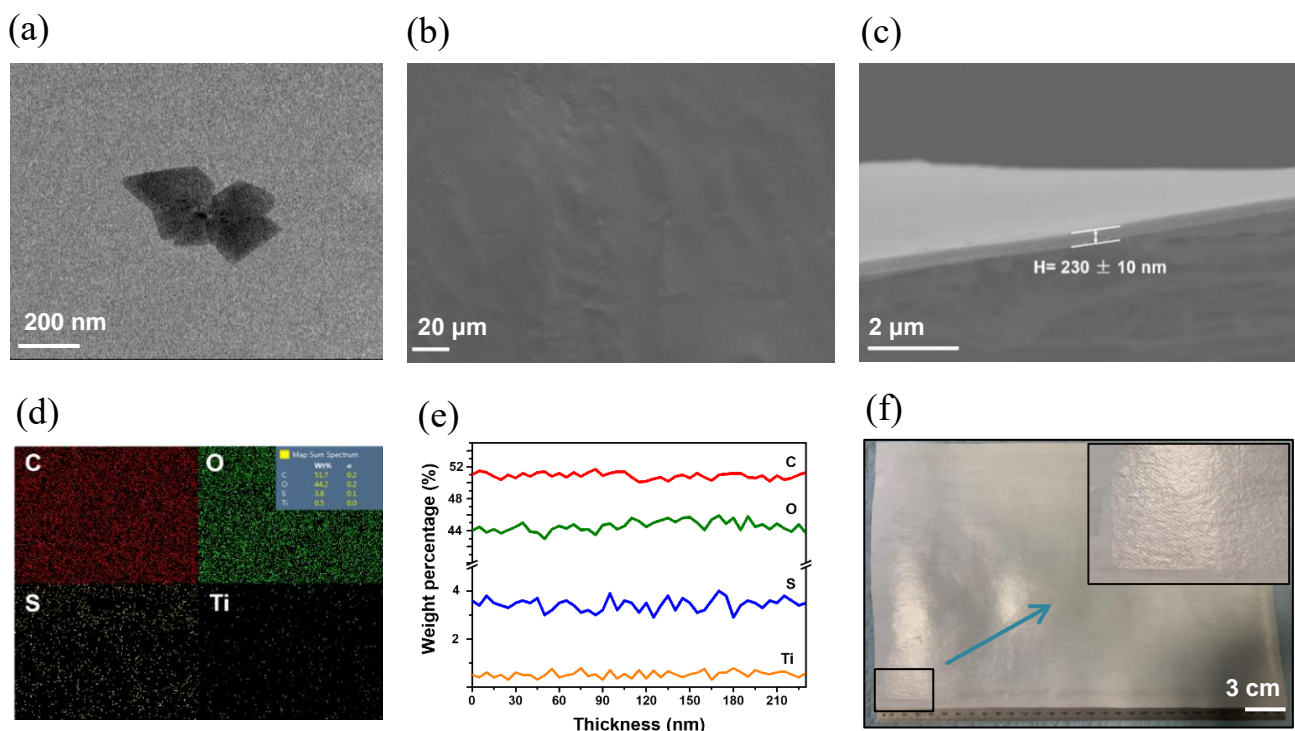
Fig. 3. (a) TEM image of several as-prepared $Ti_3C_2T_x$ MXene nanosheets with the lateral diameters in

the range of 142 ± 90 nm. Individual MXene nanosheet of such sizes can be found in Fig. S6. (b) SEM

surface view of the PSM/PTFE membrane, (c) cross-sectional image of the nanofilm composite

membrane, confirming the PVA based nanofilm thickness of $\approx$230 nm, (d) the surface EDS elemental

mapping corresponding to the PSM/PFTE membrane with uniform C, O, S and Ti distribution, (e)

EDS line scan across the cross-section of the PSM layer and (f) photograph of large-scale PSM/PTFE

membrane with magnified section (inserted) showing a thin layer on top of the substrate.
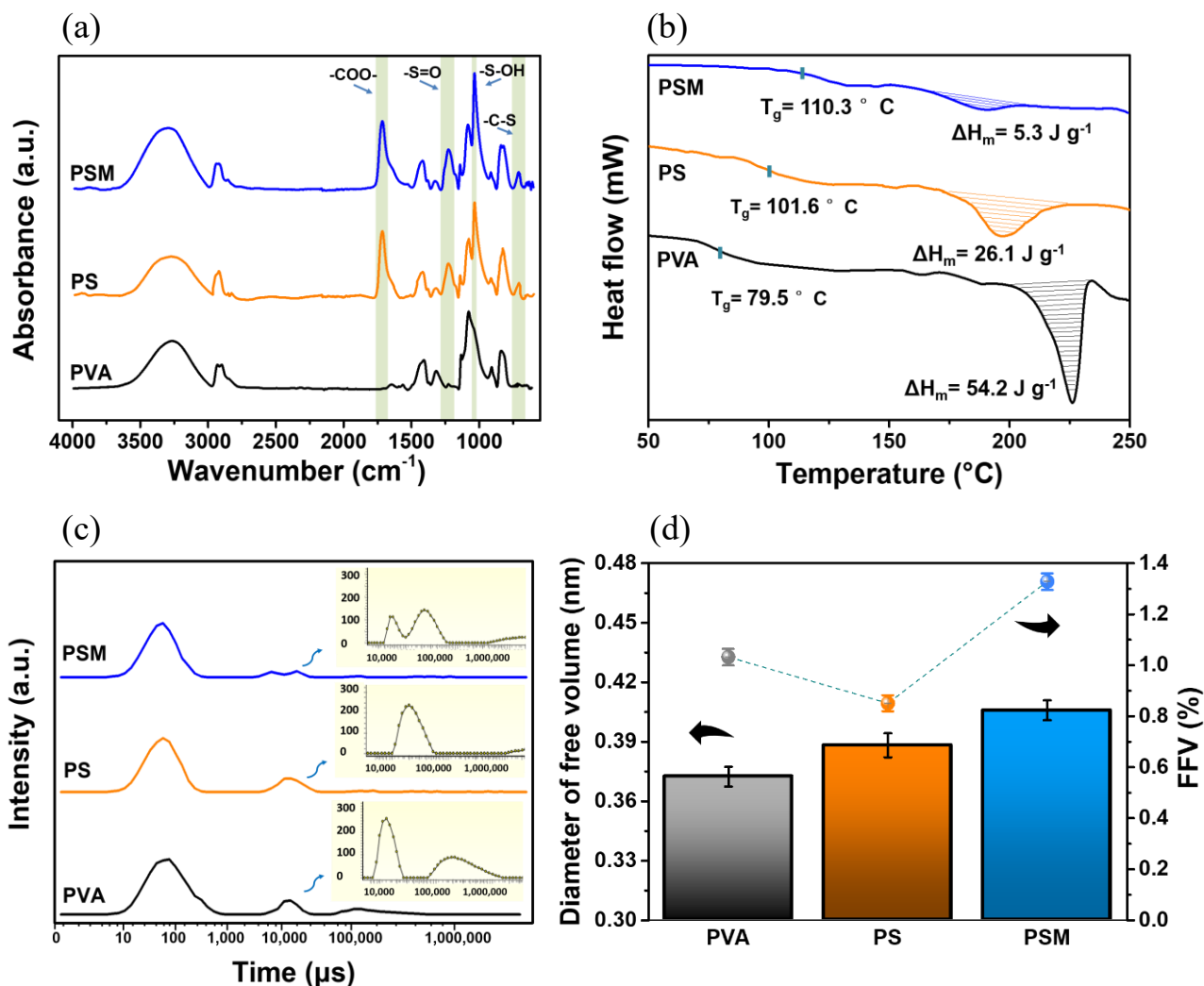
3.2. Effect of MXene on polymer matrix

The chemical functionality change that occurred during film formation was identified by ATR-

FTIR analysis as shown in Fig. 4a. Typically, the neat PVA spectrum is characterized by absorption

bands at 3260 cm^{-1} (v(O-H) from intermolecular and intramolecular hydrogen bonded hydroxyl

276   groups), 2985 and 2820 cm^{-1} (ν_{asym} and ν_{sym} (C-H) of the alkyl groups), 1450 cm^{-1} (ν(-CH$_2$-) of the

277   methylene groups from PVA backbone) and 1085 cm^{-1} (ν(C-O) of the hydroxyl groups). In contrast,

278   the PS spectrum had obvious new absorption peaks at 725, 1048, 1184 and 1725 cm^{-1} that could be

279   assigned to ν(C-S), ν(S-OH), ν(S=O) and ν(-COO-), respectively. Additionally, the peak intensities at

280   1085 and 3260 cm^{-1} decreased after the addition of SSA, indicating a diminution in the concentration

281   of hydroxyl groups. Considering such spectrum changes observed for PS, it was reasonable to conclude

282   that -COOH (from SSA) and -OH (from PVA) groups reacted via dehydration condensation for

283   carboxylic acid ester formation, resulting in SSA covalently bridged or grafted PVA. The sulfonic

284   groups were thereby linked onto the polymer chains (Fig. S12a and b). The as-prepared PSM exhibited

285   strengthened and blue-shifted (from 3260 to 3300 cm^{-1}) v(O-H) adsorption band while retaining all

286   the above-mentioned characteristic peaks for sulfonic groups and ester groups, implying that the

287   MXene nanosheet caused enhanced hydrogen bonds, possibly brought about by complex interfacial

288   interactions with PVA during annealing (Fig. S12c). Increasing MXene loading in the PVA matrix

289   might induce further dehydration condensation reactions, resulting in enhanced absorption band of

290   ester groups (Fig. S13).

291   The nanofiller-polymer interactions can be highly related to the bulk physicochemical properties

292   such as thermostability and crystallinity. Fig. 4b displays DSC thermograms of the fabricated PVA

293   based films. The glass transition temperature (T$_g$) of the neat PVA sample was 79.5°C whereas those

294   of PS and PSM rose significantly to 101.6°C and 110.3°C, respectively. The progressive elevation of

295   T$_g$ suggested reduced chain segment mobility that could be ascribed to crosslinking and nanofiller-

296   polymer interactions. On the other hand, since PVA is a semi-crystalline polymer in which there

297   coexists randomly coiled and entangled chains in the amorphous regions as well as regularly well-

packed chains in micro-domains, that partial crystalline property or the degree of crystallinity can be described by the proportion of melting enthalpy (ΔH_m) compared to that of 100% crystalline PVA ($\Delta H = 138.6$ J g^{-1}) [50]. As annotated in Fig. 4b, the melting enthalpy of neat PVA sample was 54.2 J g^{-1}, translating to a crystallinity degree of 39.1%. After the chemical reactions with SSA, the degree of crystallinity decreased to 18.8%, indicative of the annexation between the polar moieties of crosslinker and polymer interfering the local chain packing to some extent. Introducing the MXene nanosheets into the polymer matrix exhibited a sharp drop of crystallinity down to 3.8%. Such dramatic decrease primarily originated from the intimate compatibility, large 2D interfacial association with PVA and uniform dispersion in the matrix. From the DSC curve of PSM, it could be deduced that no observable phase separation took place in PSM since no shoulder-like peaks were observed, further confirming a uniform dispersion state of MXene consistent with the results of SEM EDS. To further investigate the effects of SSA and MXene on the crystalline characteristics qualitatively, XRD measurements were performed (Fig. S14). The Bragg scattering peaks centered at $2\theta = 19.5$ ° revealed the orthorhombic lattice (101) of PVA and the gradual broadening trend of their full width at half maxima (FWHM) demonstrated the continuous reduction of the crystallite size, i.e., 3.5 ± 0.1 nm (PVA), 2.3 ± 0.1 nm (PS) and 1.4 ± 0.2 nm (PSM).

Fig. 4. (a) ATR-FTIR spectra of the neat PVA, PS and PSM (PVA, PS and PSM refer to 20 μm thick, free-standing films for the material characterization), (b) DSC analysis of the neat PVA, PS and PSM sample with T_g as marked, the melting enthalpy ΔH_m plotted as filled part of each sample; (c) CPMG spectra of the neat PVA, PS and PSM, enlarged low μs range for clear comparison and (d) PALS analysis of the neat PVA, PS and PSM in terms of free volume size and FFV. Details were shown in Table S1.

The transverse (T2) relaxation time is disclosed in Carr-Purcell-Meiboom-Gill (CPMG) spectra (Fig. 4c), which represents the fast (high μs range) and slow (low μs range) motion of polymer

molecule or chains. The neat PVA sample had a T2 distribution comprising one rigid and two flexible regions centered at 100, 20 000 and 300 000 μs, respectively. The component of the sample that was more mobile was either intimately mixed with, bound to the major solid component or adsorbed on the surface. The PS showed a lower relaxation time of the flexible regions with narrower distributions and decreased intensity, indicating a reductive motion of the polymer chains. By contrast, the onset of longer T2 component in the PSM spectrum left-shifted from 10 000 to 8 000 μs with evident diminishing of the intensity relative to that of PVA and PS samples, suggesting a reduced conformational flexibility of the polymer matrix, in line with the pronounced polymer rigidification in the glass transition temperature. Moreover, the peaks in the flexible region of PSM overlapped partly, implying that possible interaction between these more mobile components induced by MXene. However, no observable interactions manifested between flexible components in PVA or PS owing to the isolated peaks. The T2 relaxation results were in good accordance with the free induction decay (FID) results (Fig. S15), which further proved the enhanced structural rigidity of PSM.

Besides the breakdown of crystalline chain arrangement and rigidification of chain segments, the intrinsic spatial structure of PSM can also be tuned by SSA and MXene. In Fig. 4d, PALS analysis revealed the average free volume diameter of PVA (0.372 nm), PS (0.388 nm) and PSM (0.406 nm) as well as the corresponding fractional free volume (FFV). The average size of free volume (PS) first increased due to the intercalation and crosslinking of SSA between PVA chains, which gave rise to a 4.3% enlargement with respect to the neat PVA. After the subsequent incorporation of $Ti_3C_2T_x$ MXene, it was further increased by 9.1% for PSM. The incremental free volume size stood for a growing gap unoccupied between the polymer chains, polymer-MXene or MXene-MXene. On the other hand, compared with neat PVA (1.032%), the polymer's FFV of PS shrank to 0.851%. That was direct

evidence of the crosslinking reaction between the PVA chains and SSA, leading to a reduction of the

total amount of free space within the polymer matrix. Notably, the PSM was measured with the highest

FFV (1.329%), that was, 28.8% and 56.2% higher than PVA and PS, respectively. As molecular

transport through the polymeric membrane is predominantly determined by the polymer nanostructure,

such elevations in both free volume size and FFV by incorporation of MXene is desirable to construct

a membrane with appropriate free volume property for enhancing permeation. Taken together with the

decrease in crystallinity, the PSM inner structure is herein proposed as shown in the schematic

illustration (Fig. S16). The nanoscale hybrid of PVA, SSA and MXene provided an altered

conformation comprising crosslinked polymer continuous phase, nanofiller dispersed phase and

nanofiller-polymer interphase rather than the simple polymer phase with crystallization in neat PVA.

In particular, the multiphase generated by MXene in PSM enabled higher structural rigidity with more

free space (fractional free volume) as evidenced by the above-mentioned DSC, NMR and PALS

characterizations.

The equilibrium swelling of the free-standing films wetted by water exhibited a successive

decrease, namely 283% for neat PVA, 80% for PS and 48% for PSM (Fig. 5a). The propensity of the

PVA chains to swell was predominantly suppressed due to the ester linkage existing in PS.

Comparatively, the embedded MXene nanosheets further restrained the swelling by reducing the

segmental chain mobility as evidenced in the DSC and NMR relaxation results. In Fig. 5b, the zeta

potential analysis revealed the as-fabricated composite membrane surfaces with electronegative

properties. More specifically, the PVA/PTFE membrane exhibited zeta potentials from -0.2 to -8.5 mV

throughout the pH range of 3-11. For the PS/PTFE membrane, its lower values decreased with pH and

reached -76.3 mV at pH of 11. The enhanced negativity mainly resulted from the deprotonation of the

367 sulfonic groups grafted on the membrane surface. Since MXene nanosheets were electronegative, the

368 PSM was more negative than PS owing to the contribution from the outermost MXene distributed on

369 the surface. Further, water contact angle (WCA) measurements were performed to compare the

370 wettability of the composite membranes. As shown in Fig. 5c, the increased WCA for PS/PTFE

371 membrane was due to the consumption of hydrophilic -OH groups during the crosslinking reaction.

372 The WCA of PSM (61.1°) was lower than that of PS (84.3°) and approached the neat PVA (50.3°),

373 suggesting that the MXene nanosheets were able to provide hydrophilic groups on the nanofilm surface

374 despite the consumed hydroxyl groups of PVA during ester formation with SSA. Furthermore, the

375 WCA of the substrate showed hydrophobicity (155.5° of PTFE layer), confirming the Janus property
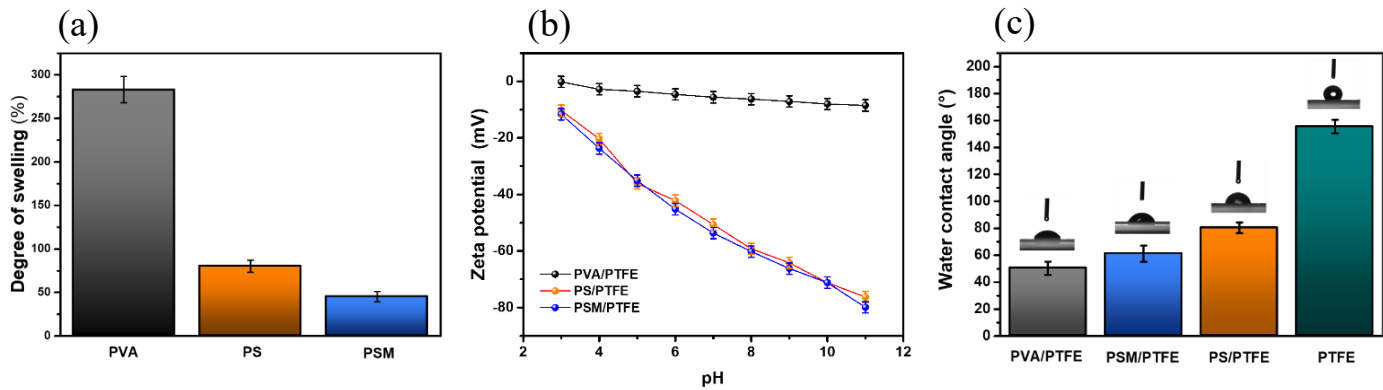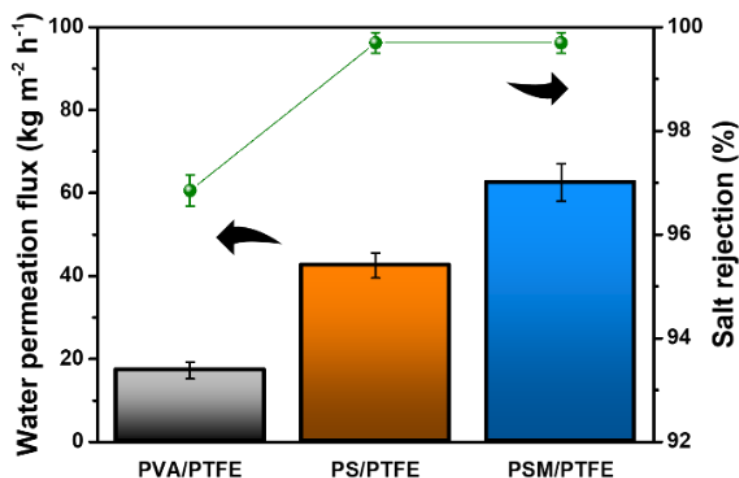
376 of the composite membranes.

377 **Fig. 5.** (a) Swelling of the PVA based hybrids, (b) surface charge of the composite membranes and (c)

378 water contact angles of the composite membranes and substrate.

379 *3.3. Performance evaluation of the nanofilm composite membranes*

380   *3.3.1. Enhanced separation performances by transport agents and MXene nanosheets*

381

382   **Fig. 6.** Separation performances of the synthesized composite membranes.

383

384   To evaluate and compare the separation performances of the fabricated membranes, PV

385   desalination at 30 °C using 0.6 M (3.5 wt%) NaCl solution was performed on PVA/PTFE, PS/PTFE

386   and PSM/PTFE composites as presented in Fig. 6. The water trans-membrane flux was gradually

387   elevated by the incorporation of SSA and subsequent MXene nanosheets, increasing from 17.5 kg m^{-2}

388   h^{-1} (PVA/PTFE) to 45.7 (PS/PTFE) and 62.2 kg m^{-2} h^{-1} (PSM/PTFE). These are equivalent to 1.6- and

389   2.6-fold enhancements of water permeation flux, respectively. In addition, the PS/PTFE and

390   PSM/PTFE exhibited almost complete salt rejection (99.8%) whereas the PVA/PTFE was unable to

391   prevent ions from penetrating through. The microporous PTFE membrane is well known for its high

392   salt rejection as a membrane distillation membrane due to its hydrophobic property. However, under

393   the same operating condition used for PSM, the separating performance of PP supported PTFE

394   substrate was found to be inferior possibly due to membrane wetting under the high vacuum used (Fig.

395   S17). Hence, the PVA based hybrids determined the separation properties. In general, the impermeable

396   crystallites of PVA significantly impede water transport through the membrane due to highly ordered

397 alignment of polymer chains whereas the amorphous region is responsible for the permeation behavior

398 of solutes. The amorphous-to-crystalline ratio of the bulk PVA underwent obvious increases as

399 evidenced by DSC, indicating that the PS and PSM were more permeable relative to PVA, in agreement

400 with previous literature [48, 51, 52]. For the PS separating layer, despite the reduced FFV of its

401 crosslinked framework with respect to neat PVA, the enlarged size of free volume possessed lower

402 mass transfer resistance. Simultaneously, the sulfonic acid groups, featuring facilitated transporters,

403 could also accelerate water permeation to realize such fast transport property of PS. Compared with

404 PS/PTFE, MXene imparted the PSM/PTFE membrane with even higher water permeation flux because

405 of a combination of factors such as more amorphous region, increased free volume pore size, higher

406 FFV and potentially additional permeating paths through MXene or MXene-polymer interphase (will

407 be discussed later). Besides, PSM exhibited a more hydrophilic surface than PS. That indicated a higher

408 concentration of water adsorbed on the membrane surface, causing a greater concentration gradient

409 across the membrane and thus the corresponding driving force for molecule permeation.

410 On the other hand, the selectivity and stability of membranes are highly susceptible to polymer

411 chain mobility. Penetrating solutes such as water can exert solvating effect or plasticization on polymer,

412 disrupting the interchain interactions and thereby enhancing the permeation of undesired solutes.

413 Tailoring the interfacial interactions to restrain polymer structural relaxation while creating more free

414 volume, as occurred on incorporation of MXene demonstrated an effective strategy to bestow the PSM

415 with excellent separation property and stability. To further verify that, 50-hour desalination tests were

416 conducted as shown in Fig. S18. The water permeation flux of PVA/PTFE increased with time whilst

417 its salt rejection declined, possibly because of the impermanent structural configuration brought about

418 by plasticization of polymer chains and dissolution of crystallites, thus damaging the integrity and thus

419   separation performance. Crosslinking made the PVA network of PS/PTFE membrane insoluble in

420   water, resulting in an evident improvement of stability with decreased performance emerging after 35

421   h. By contrast, the PSM/PTFE membrane maintained a more stable throughput without attenuation in

422   molecule separation, providing mechanically robust and structurally stable separating nanohybrid

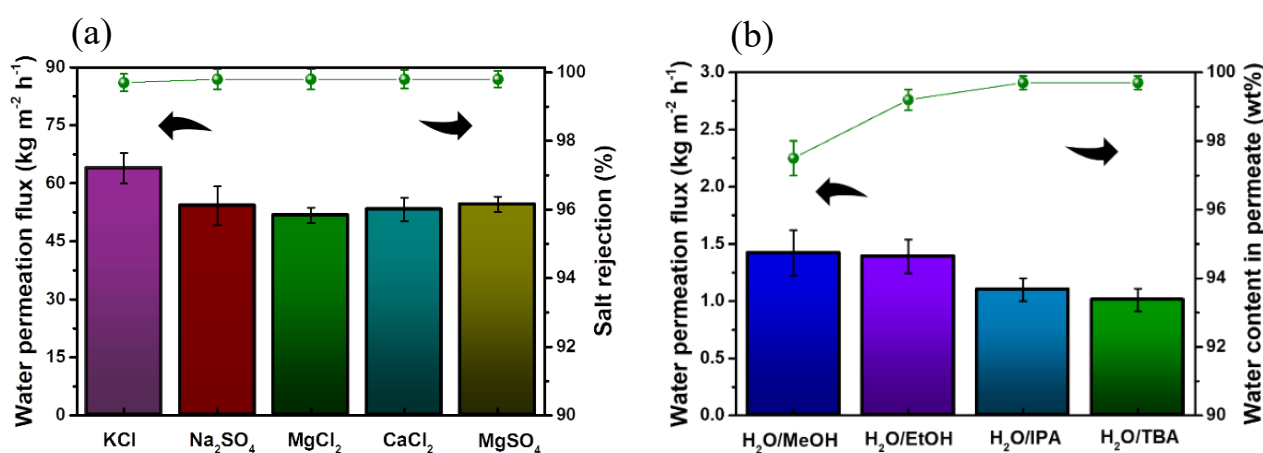423   under continuous operation.

424   **Fig. 7.** Separation performances of PSM/PTFE for (a) PV desalination and (b) solvent dehydration.
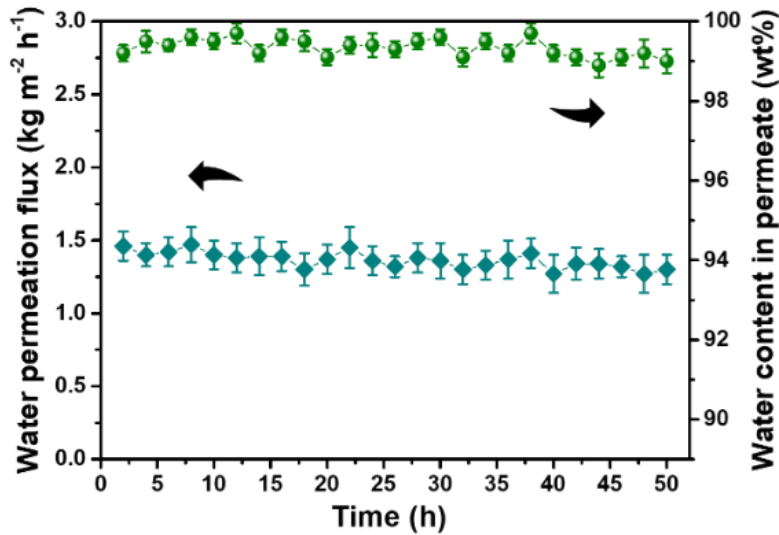
425   Since the PSM/PTFE membrane exhibited superior separation performance to PVA/PTFE and

426   PS/PTFE, its molecular separation properties were further probed by pervaporative separations of

427   water from various aqueous ion or alcohol solutions. In Fig. 7a, the desalination performances toward

428   various salt solutions are presented. The PSM/PTFE composite membrane exhibited high salt

429   rejections, i.e., 99.81% (KCl), 99.91%(Na$_2$SO$_4$), 99.93% (MgCl$_2$), 99.92% (CaCl$_2$) and 99.93%

430   (MgSO$_4$). Apart from the specific nanostructure and intrinsic affinity with water, the PSM/PTFE

431   showed a negatively charged surface (Fig.4b), which was beneficial for ion rejection according to the

432   Donnan exclusion effect [53]. Further, divalent ions are more sensitive to the charge exclusion than

433   monovalent ions. In order to keep charge neutrality, cation-anion couple stayed in stoichiometric

balance. Therefore, higher salt rejections were achieved for those divalent ions. However, minor variation in the water permeation fluxes from 63.9 to 58.7 kg m^{-2} h^{-1} was discerned, suggesting that various ions in solution affected water adsorption on the membrane surface. With increased solvated ion radii, hydration number and total concentrations of ions (Table S2), free water molecules that would be dissolved on the membrane surface were suspected to decrease, which influenced the total trans-membrane flux.

As demonstrated in our previous study [54], PV desalination differed from dehydration of alcohols due to various effects of feed on the membrane (e.g., membrane swelling in water and swelling resistant in alcohol) and the different transport mechanisms of ions and alcohols (e.g., hydrated ions transport vs. hydrogen bonding transport of alcohols). Thus, dehydration of alcohol/water binary mixtures was carried out at 30 °C to further identify the separation property of PSM/PTFE (Fig. 7b). The C1 to C4 alcohols were readily held back whereas high purity water in the permeate stream was obtained, i.e., 97.6 (methanol/H$_2$O), 99.5 (ethanol/H$_2$O), 99.7 (propanol/H$_2$O) and 99.9 (butanol/H$_2$O) wt%. That resulted in the separation factors of 968, 4738, 7913 and 23786, respectively. Dehydration of industrial water/propanol or butanol azeotropes was also performed (Fig.S19). Similarly, the sizes of alcohol molecules also played a role in effecting the water permeation flux, similar to the role of hydrated ions in membrane based desalination process. Molar volume and average dynamic cross-section sizes of those alcohols (Table S3) demonstrated their steric hindrance to water adsorption on the membrane surface. 50-hour dehydration of ethanol was also conducted to further assess the durability of PSM/PTFE. As shown in Fig. 8, the water permeation flux slightly decreased from 1.46 to 1.31 kg m^{-2} h^{-1} during the operation, which might be caused by the reduction of water concentration in the feed tank with time. The corresponding water content in the permeate side maintained relatively
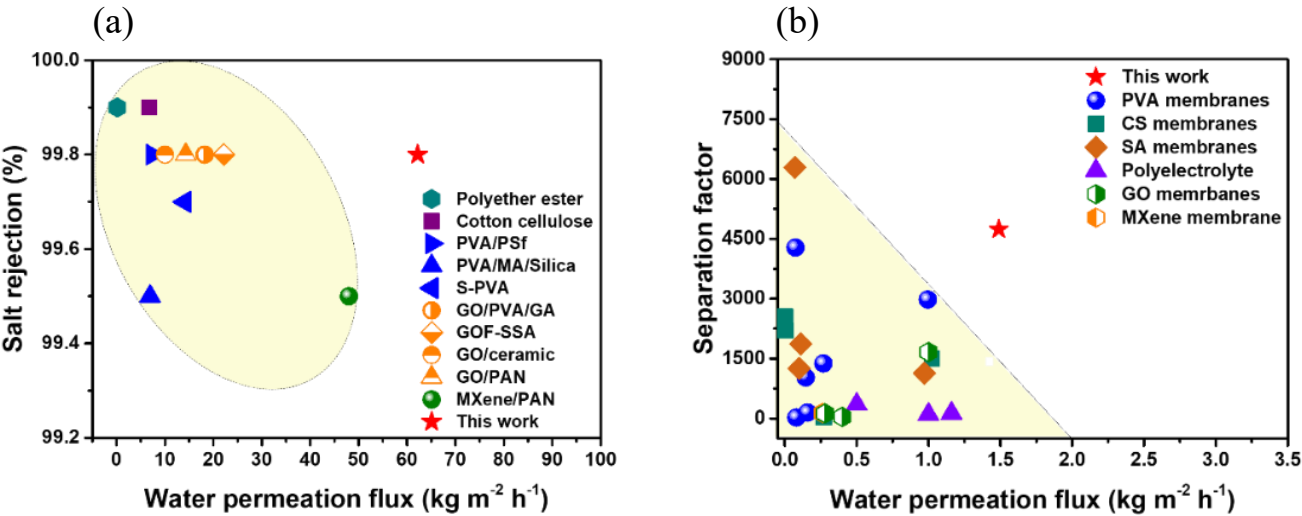
steady in the range of 99.5 to 99 wt%.

Fig. 8. 50-hour ethanol dehydration by PSM/PTFE membrane.

By comparing the separation performance with other reported membranes in PV desalination or ethanol dehydration (Fig. 9a and b), the PSM/PTFE membrane showed notably higher water permeation flux without compromising separation efficiency, placing it in a region away from the intrinsic capability of those state-of-the-art membranes (in the colored realm). Particularly for desalination, the water permeation flux was even 8.41, 4.35 and 1.29 folds of PVA/PSf (100-nm-thick maleic acid crosslinked PVA active layer) [55], GO/PAN [12] and MXene/PAN [31], respectively. As opposed to those hydrophilic substrates used in those reported PV composite membranes, the PTFE substrate here was hydrophobic and it only allowed the transport of water vapor rather than liquid. Hence it was reasonable to infer that the PV by PSM/PTFE membrane with such Janus property combined the solution-diffusion process of the PSM layer with the fast vapor transport through PTFE

469   substrate layer, which benefited the overall mass transport through the composite membrane.

470

471   **Fig. 9.** (a) Comparison of the pervaporation desalination performance under similar conditions

472   (0.6 M NaCl as feed, 30 °C, 130 Pa) [31, 56, 57] and (b) comparison of ethanol dehydration

473   performance of different kinds of membranes (PVA based, CS based, SA based, GO based and MXene

474   membrane). Shaded regions are to guide the eye. Detailed information of ethanol dehydration

475   comparison is shown in Table S4.

476   *3.3.2. Transport modelling of the composite membranes*

477   It is of major interest as to how MXene affects water transport apart from tuning the polymer with

478   high separation properties. There have been several transport models (Flory-Huggins model, pore-flow

479   model, solution-diffusion model, etc.) describing sorption and mass transport through membranes [58-
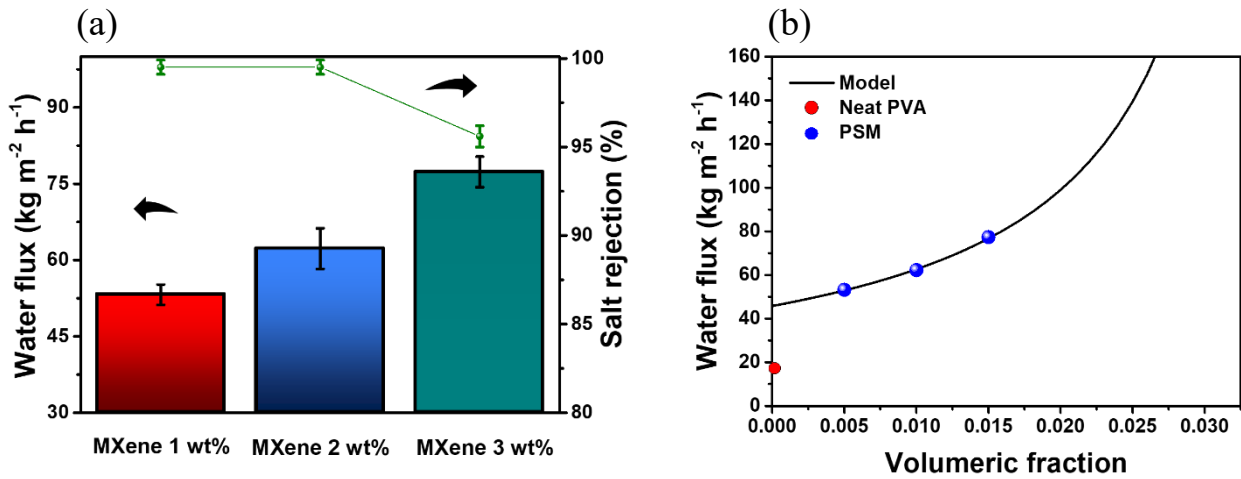
480   61]. MXene is in the shape of platelets and some transport models of MMMs account for different

481   types of nanofillers. However, considering the ratio of particle shape and size versus membrane

482   thickness, most models do not apply when the platelet length approaches the same magnitude of the
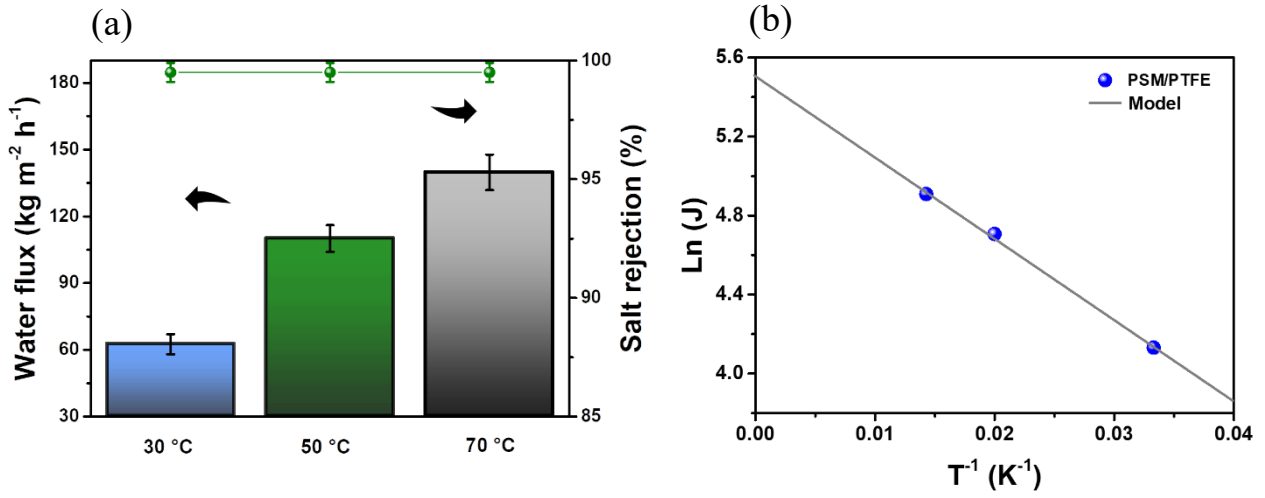
483　membrane thickness. As noted by Bhatia et al., the Chiew-Glandt model described flux well for particle

484　size (r) to membrane thickness (l) ratios (r/l) less than 0.004, and the Monsalve-Bravo and Bhatia

485　(MB-B) model described flux well for the ratios $0.004 \leq r/l \leq 0.16$ [62]. Considering that the MXene

486　particle sizes (sheet length of ≈142 nm) and membrane thickness of ≈ 230 nm resulted in a r/l ratio of

487　≈0.62, none of the above MMM models could describe the observed behavior. At these high ratios, it

488　is believed that surface effects dominated the bulk properties. In this case, the MXene nanosheets might

489　be capable of achieving a percolation threshold where the 2D-shaped channels between the nanosheets

490　and the polymer provided ultrafast transport pathways directly from the upstream to the downstream

491　surface with low resistance. To test this hypothesis, the standard RIS transport model was modified

492　with a volume fraction scaling factor (v_s) to capture the critical volume fraction at which percolation

493　was achieved (see Eq. 7). Note this percolation point is typically assumed at a volume fraction of 1

494　where the filler is the only material in the membrane. The RIS transport model predicts water flux (J_w)

495　as a function of the permeation through the filler (P_f), permeation through the polymer (P_p) and the

496　volume fraction of the filler (v_f) in Eq. 7. Fig. 10a and b show the model fit to the experimental data

497　for PSM/PTFE at various MXene contents, resulting in an excellent fit with a coefficient of

498　determination $R^2 = 0.9989$ and root-mean-squared-error (RMSE) = 0.33. All parameters were fitted

499　part from the filler volume fraction v_f. Note that PVA without filler was not included in this fit. A very

500　sharp rise at low volume concentrations < 0.02 (2 %) is observed as the filler creates ultra-fast pathways

501　over a thousand times faster than for the polymer ($P_f = 68\ 791$ and $P_p = 45.79$ kg m^{-2} h^{-1}). According

502　to this model, the percolation threshold is reached at a volume fraction of 0.037 (3.7%) where a

503　continuous pathway is established from upstream to downstream that completely dominates above any

504　transport rates through the bulk polymer. Assuming an Arrhenius relationship between flux J_w and

505 temperature T, the activation energy ΔE was calculated using Eq. 8. Fig.11a and b display the model

506 fit to the experimental data for PVA-Mxene at 2 wt% gravimetric loading (1% volumetric loading) at

507 30, 50 and 70 °C. The activation energy ΔE was estimated as 0.082 kcal mol^{-1}, which is considered

508 low compared to the hydrogen bonding strength between water molecules of around 5 kcal mol^{-1} [63].

509 This means that there is low resistance for water transport through the membrane in agreement with

510 the RIS transport model. Fig. 12 illustrates how the film thickness (l) and the size of the filler (r) can

511 affect the total flux through the membrane. At high r/l ratios (Fig. 12b), the standard MMM models do

512 not apply as there exists a percolation threshold capable of drastically increasing the total flux by

513 opening up the pathways with minimal resistance. As shown by the RIS and Arrhenius models, the

514 water flux is extremely high through the filler regions at 68 791 kg m^{-2} h^{-1} (relative to 45.79 kg m^{-2} h^{-}

515 ^{1} through the PVA polymer regions) with a low activation energy of 0.082 kcal mol^{-1} compared with
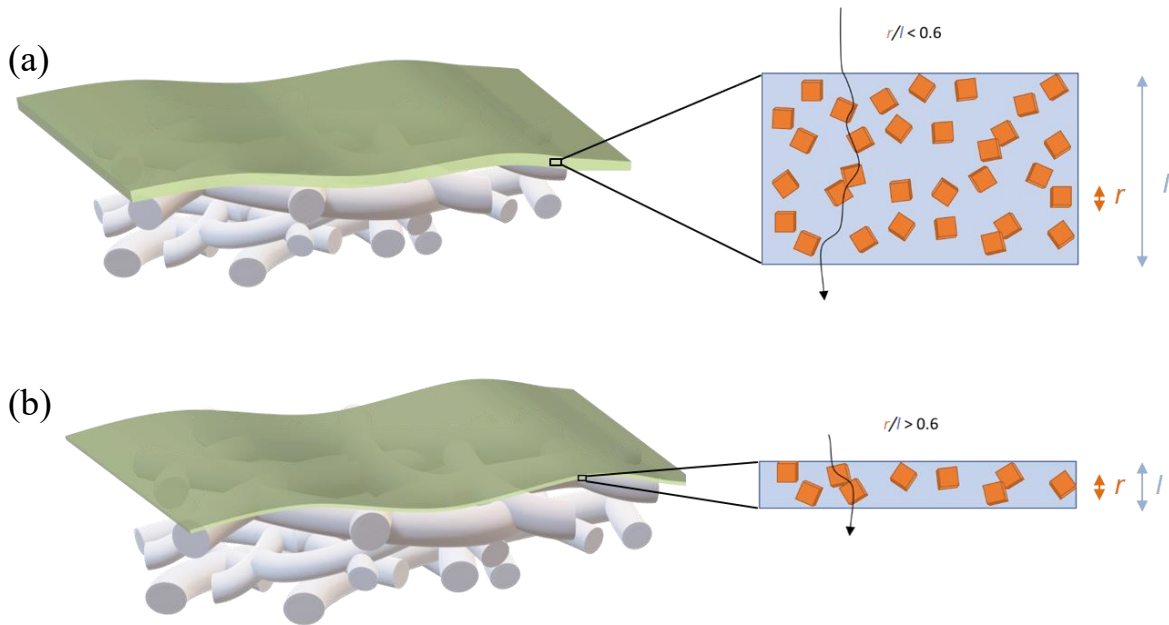
516 5.21 kcal mol^{-1} for PVA [64].

517 **Fig. 10.** PV performances of PSM/PTFE and its transport modelling fit. (a) Performance of PSM/PTFE

518 at various MXene contents in desalination (0.6 M NaCl solution) at 30 °C and (b) the modified RIS

519 model fit. Fitted values include P_p = 45.79, P_f = 68,791 and v_s = 0.0372. The water permeation flux

520 increased with MXene loading. However, at 3 wt% MXene loading, the salt rejection decreased,

521   indicating that a trade-off effect occurred.

522   **Fig. 11.** Performance of PSM/PTFE at various feed temperatures. (a) Water flux and salt rejection for

523   desalination (NaCl) process at 30, 50 and 70 °C. (b) Arrhenius relationship with fitted values including

524    $A = 247.2$ kg m^{-2} h^{-1} and $\Delta E = 0.082$ kcal/mol using Eq. 8.

525

526

527   **Fig. 12.** Schematic of filler size (r) and membrane thickness (l) effecting the resistance of transport

528   through the membrane. (a) when $r/l < 0.6$, solutes permeate through polymer-nanofiller multiphase;

(b) when $r/l > 0.6$, there exists a percolation threshold at a filler fraction that creates a pathway with minimal resistance.

4. Conclusions

We developed a high-performance PVA based hybrid material and realized the fabrication of intrusion-free layer on a hydrophobic microporous substrate by a scalable solution casting strategy. Importantly, greatly enhanced water permeation was not accompanied with a decrease in selectivity after the incorporation of a relativity small amount of 2D MXene in the crosslinked PVA matrix, which was underpinned by the MXene-induced polymer rigidification, crystalline reduction, free volume elevation and fast transport pathways. It demonstrated that the PSM/PTFE membrane exhibited outstanding separation capacity with stability for a wide range of water/salt and water/alcohol mixtures, setting this membrane apart from state-of-the-art membranes for use of PV. Additional advantage of the PSM/PTFE composite can be ascribed to its facile and rapid solution casting process for large-area fabrication leveraged to industrial-scale demand. This work provides a rational design for nanohybrid membranes which is not limited to the 2D nanofiller incorporated membranes but also potentially applicable for other dimensional fillers such as nanoparticles and porous nanomaterials.

References

550

551 [1] P. Shao, R.Y.M. Huang, Polymeric membrane pervaporation, J. Membr. Sci. 287 (2007) 162-179.

552 [2] P.D. Chapman, T. Oliveira, A.G. Livingston, K. Li, Membranes for the dehydration of solvents by pervaporation, J.
553   Membr. Sci. 318 (2008) 5-37.

554 [3] X. Feng, R.Y.M. Huang, Liquid Separation by Membrane Pervaporation: A Review, Ind. Eng. Chem. Res. 36 (1997)
555   1048-1066.

556 [4] X. Cheng, F. Pan, M. Wang, W. Li, Y. Song, G. Liu, H. Yang, B. Gao, H. Wu, Z. Jiang, Hybrid membranes for
557   pervaporation separations, J. Membr. Sci. 541 (2017) 329-346.

558 [5] B. Smitha, D. Suhanya, S. Sridhar, M. Ramakrishna, Separation of organic–organic mixtures by pervaporation—a
559   review, J. Membr. Sci. 241 (2004) 1-21.

560 [6] Q. Wang, N. Li, B. Bolto, M. Hoang, Z. Xie, Desalination by pervaporation: A review, Desalination 387 (2016) 46-60.

561 [7] A.W. Mohammad, Y.H. Teow, W.L. Ang, Y.T. Chung, D.L. Oatley-Radcliffe, N. Hilal, Nanofiltration membranes review:
562   Recent advances and future prospects, Desalination 356 (2015) 226-254.

563 [8] C. Fritzmann, J. Löwenberg, T. Wintgens, T. Melin, State-of-the-art of reverse osmosis desalination, Desalination 216
564   (2007) 1-76.

565 [9] A. Alkhudhiri, N. Darwish, N. Hilal, Membrane distillation: A comprehensive review, Desalination 287 (2012) 2-18.

566 [10] H. Zwijnenberg, G. Koops, M. Wessling, Solar driven membrane pervaporation for desalination processes, J. Membr.
567   Sci. 250 (2005) 235-246.

568 [11] M. Naim, M. Elewa, A. El-Shafei, A. Moneer, Desalination of simulated seawater by purge-air pervaporation using an
569   innovative fabricated membrane, Water Sci. Technol. 72 (2015) 785-793.

570 [12] B. Liang, W. Zhan, G. Qi, S. Lin, Q. Nan, Y. Liu, B. Cao, K. Pan, High performance graphene oxide/polyacrylonitrile
571   composite pervaporation membranes for desalination applications, J. Mater. Chem. A 3 (2015) 5140-5147.

572 [13] M. Drobek, C. Yacou, J. Motuzas, A. Julbe, L. Ding, J.C. Diniz da Costa, Long term pervaporation desalination of
573   tubular MFI zeolite membranes, J. Membr. Sci. 415-416 (2012) 816-823.

574 [14] X. Qian, N. Li, Q. Wang, S. Ji, Chitosan/graphene oxide mixed matrix membrane with enhanced water permeability
575   for high-salinity water desalination by pervaporation, Desalination 438 (2018) 83-96.

576 [15] F. Ugur Nigiz, Graphene oxide-sodium alginate membrane for seawater desalination through pervaporation,
577   Desalination 485 (2020) 114465-114475.

578 [16] V. Van Hoof, L. Van den Abeele, A. Buekenhoudt, C. Dotremont, R. Leysen, Economic comparison between azeotropic
579   distillation and different hybrid systems combining distillation with pervaporation for the dehydration of isopropanol,
580   Sep. Purif. Technol. 37 (2004) 33-49.

581 [17] A. Verhoef, J. Degrève, B. Huybrechs, H. van Veen, P. Pex, B. Van der Bruggen, Simulation of a hybrid pervaporation–
582   distillation process, Comput. Chem. Eng. 32 (2008) 1135-1146.

583 [18] A. Jonquières, R. Clément, P. Lochon, J. Néel, M. Dresch, B. Chrétien, Industrial state-of-the-art of pervaporation
584   andvapour permeation in the western countries, J. Membr. Sci. 206 (2002) 87–117.

585 [19] B. Bolto, M. Hoang, Z. Xie, A review of membrane selection for the dehydration of aqueous ethanol by pervaporation,
586   Chemical Engineering and Processing: Process Intensification 50 (2011) 227-235.

587 [20] G. Liu, W. Jin, N. Xu, Graphene-based membranes, Chem. Soc. Rev. 44 (2015) 5016-5030.

588 [21] T.C. Bowen, R.D. Noble, J.L. Falconer, Fundamentals and applications of pervaporation through zeolite membranes,
589   J. Membr. Sci. 245 (2004) 1-33.

590 [22] X. Liu, H. Jin, Y. Li, H. Bux, Z. Hu, Y. Ban, W. Yang, Metal–organic framework ZIF-8 nanocomposite membrane for
591   efficient recovery of furfural via pervaporation and vapor permeation, J. Membr. Sci. 428 (2013) 498-506.

592 [23] Z. Xie, D. Ng, M. Hoang, J. Zhang, S. Gray, Study of Hybrid PVA/MA/TEOS Pervaporation Membrane and

593   Evaluation of Energy Requirement for Desalination by Pervaporation, Int. J. Environ. Res. Public Health 15 (2018)
594   1913-1931.

595 [24] B. Bolto, T. Tran, M. Hoang, Z. Xie, Crosslinked poly(vinyl alcohol) membranes, Prog. Polym. Sci. 34 (2009) 969-
596   981.

597 [25] B. Liang, Q. Li, B. Cao, P. Li, Water permeance, permeability and desalination properties of the sulfonic acid
598   functionalized composite pervaporation membranes, Desalination 433 (2018) 132-140.

599 [26] R. Zhang, B. Liang, T. Qu, B. Cao, P. Li, High-performance sulfosuccinic acid cross-linked PVA composite
600   pervaporation membrane for desalination, Environ. Technol. (2017) 1-9.

601 [27] Y.l. Xue, C.H. Lau, B. Cao, P. Li, Elucidating the impact of polymer crosslinking and fixed carrier on enhanced water
602   transport during desalination using pervaporation membranes, J. Membr. Sci. 575 (2019) 135-146.

603 [28] Y. Wu, L. Ding, Z. Lu, J. Deng, Y. Wei, Two-dimensional MXene membrane for ethanol dehydration, J. Membr. Sci.
604   590 (2019) 117300-117308.

605 [29] Z. Xu, G. Liu, H. Ye, W. Jin, Z. Cui, Two-dimensional MXene incorporated chitosan mixed-matrix membranes for
606   efficient solvent dehydration, J. Membr. Sci. 563 (2018) 625-632.

607 [30] L. Ding, Y. Wei, L. Li, T. Zhang, H. Wang, J. Xue, L.X. Ding, S. Wang, J. Caro, Y. Gogotsi, MXene molecular sieving
608   membranes for highly efficient gas separation, Nat Commun 9 (2018) 155-162.

609 [31] G. Liu, J. Shen, Q. Liu, G. Liu, J. Xiong, J. Yang, W. Jin, Ultrathin two-dimensional MXene membrane for
610   pervaporation desalination, J. Membr. Sci. 548 (2018) 548-558.

611 [32] K.C. Khulbe, T. Matsuura, Thin Film Composite and/or Thin Film Nanocomposite Hollow Fiber Membrane for Water
612   Treatment, Pervaporation, and Gas/Vapor Separation, Polymers (Basel) 10 (2018).

613 [33] S. Karan, Z. Jiang, A.G. Livingston, Sub–10 nm polyamide nanofilms with ultrafast solvent transport for molecular
614   separation, Science 348 (2015) 1347-1351.

615 [34] W.J. Lau, A.F. Ismail, N. Misdan, M.A. Kassim, A recent progress in thin film composite membrane: A review,
616   Desalination 287 (2012) 190-199.

617 [35] N. Misdan, W.J. Lau, A.F. Ismail, T. Matsuura, Formation of thin film composite nanofiltration membrane: Effect of
618   polysulfone substrate characteristics, Desalination 329 (2013) 9-18.

619 [36] L. Shi, S.R. Chou, R. Wang, W.X. Fang, C.Y. Tang, A.G. Fane, Effect of substrate structure on the performance of
620   thin-film composite forward osmosis hollow fiber membranes, J. Membr. Sci. 382 (2011) 116-123.

621 [37] S. Sahebi, S. Phuntsho, Y.C. Woo, M.J. Park, L.D. Tijing, S. Hong, H.K. Shon, Effect of sulphonated polyethersulfone
622   substrate for thin film composite forward osmosis membrane, Desalination 389 (2016) 129-136.

623 [38] P. Li, H.Z. Chen, T.-S. Chung, The effects of substrate characteristics and pre-wetting agents on PAN–PDMS
624   composite hollow fiber membranes for CO2/N2 and O2/N2 separation, J. Membr. Sci. 434 (2013) 18-25.

625 [39] J.M.S. Henis, M.K. Tripodi, Composite hollow fiber membranes for gas separation: the resistance model approach, J.
626   Membr. Sci. 8 (1981) 233-246.

627 [40] N. Wang, S. Ji, J. Li, R. Zhang, G. Zhang, Poly(vinyl alcohol)–graphene oxide nanohybrid "pore-filling" membrane
628   for pervaporation of toluene/n-heptane mixtures, J. Membr. Sci. 455 (2014) 113-120.

629 [41] A.B.D. Cassie, S. Baxter, Wettability of porous surfaces, Trans. Faraday Soc. 40 (1944) 546-551.

630 [42] H.Z. Chen, Y.C. Xiao, T.-S. Chung, Multi-layer composite hollow fiber membranes derived from poly(ethylene glycol)
631   (PEG) containing hybrid materials for CO2/N2 separation, J. Membr. Sci. 381 (2011) 211-220.

632 [43] S.Y. Park, J.W. Chung, S.-Y. Kwak, Regenerable anti-fouling active PTFE membrane with thermo-reversible "peel-
633   and-stick" hydrophilic layer, J. Membr. Sci. 491 (2015) 1-9.

634 [44] Y. Wang, Y. Hu, J. Xu, G. Luo, Y. Dai, Immobilization of lipase with a special microstructure in composite hydrophilic
635   CA/hydrophobic PTFE membrane for the chiral separation of racemic ibuprofen, J. Membr. Sci. 293 (2007) 133-141.

636 [45] Z. Bi, D.W. Mueller, Friction predication on pin-to-plate interface of PTFE material and steel, Friction 7 (2018) 268-

281.

[46] A. Akbari, P. Sheath, S.T. Martin, D.B. Shinde, M. Shaibani, P.C. Banerjee, R. Tkacz, D. Bhattacharyya, M. Majumder, Large-area graphene-based nanofiltration membranes by shear alignment of discotic nematic liquid crystals of graphene oxide, Nat Commun 7 (2016) 10891-10903.

[47] Z. Xie, M. Hoang, T. Duong, D. Ng, B. Dao, S. Gray, Sol–gel derived poly(vinyl alcohol)/maleic acid/silica hybrid membrane for desalination by pervaporation, J. Membr. Sci. 383 (2011) 96-103.

[48] F. Peng, F. Pan, H. Sun, L. Lu, Z. Jiang, Novel nanocomposite pervaporation membranes composed of poly(vinyl alcohol) and chitosan-wrapped carbon nanotube, J. Membr. Sci. 300 (2007) 13-19.

[49] D.-Y. Kim, J.-G. Lee, B.N. Joshi, S.S. Latthe, S.S. Al-Deyab, S.S. Yoon, Self-cleaning superhydrophobic films by supersonic-spraying polytetrafluoroethylene–titania nanoparticles, J. Mater. Chem. A 3 (2015) 3975-3983.

[50] B. Wang, Z. Chen, J. Zhang, J. Cao, S. Wang, Q. Tian, M. Gao, Q. Xu, Fabrication of PVA/graphene oxide/TiO2 composite nanofibers through electrospinning and interface sol–gel reaction: Effect of graphene oxide on PVA nanofibers and growth of TiO2, Colloids and Surfaces A: Physicochemical and Engineering Aspects 457 (2014) 318-325.

[51] G. Li, W. Zhang, J. Yang, X. Wang, Time-dependence of pervaporation performance for the separation of ethanol/water mixtures through poly(vinyl alcohol) membrane, J. Colloid Interface Sci. 306 (2007) 337-344.

[52] S. Xu, L. Shen, C. Li, Y. Wang, Properties and pervaporation performance of poly(vinyl alcohol) membranes crosslinked with various dianhydrides, J. Appl. Polym. Sci. 135 (2018) 46159.

[53] P. Schaetzel, E. Favre, Q.T. Nguyen, J. Neel, Mass transfer analysis of pervaporation through an ion exchange membrane, Desalinution 90 (1993) 259-276.

[54] G. Yang, Z. Xie, C.M. Doherty, M. Cran, D. Ng, S. Gray, Understanding the transport enhancement of poly (vinyl alcohol) based hybrid membranes with dispersed nanochannels for pervaporation application, J. Membr. Sci. 603 (2020) 118005.

[55] S.G. Chaudhri, B.H. Rajai, P.S. Singh, Preparation of ultra-thin poly(vinyl alcohol) membranes supported on polysulfone hollow fiber and their application for production of pure water from seawater, Desalination 367 (2015) 272-284.

[56] Z. Xie, D. Ng, M. Hoang, T. Duong, S. Gray, Separation of aqueous salt solution by pervaporation through hybrid organic–inorganic membrane: Effect of operating conditions, Desalination 273 (2011) 220-225.

[57] G. Yang, Z. Xie, M. Cran, D. Ng, C.D. Easton, M. Ding, H. Xu, S. Gray, Functionalizing graphene oxide framework membranes with sulfonic acid groups for superior aqueous mixture separation, J. Mater. Chem. A 7 (2019) 19682-19690.

[58] J.G. Wijmans, R.W. Baker, The solution-diffusion model: a review, J. Membr. Sci. 107 (1995) 1-21.

[59] F. Lipnizki, G. Trägårdh, Modelling of Pervaporation: Models to Analyze and Predict the Mass Transport in Pervaporation, Sep. Purif. Methods 30 (2007) 49-125.

[60] P. Sukitpaneenit, T.-S. Chung, L.Y. Jiang, Modified pore-flow model for pervaporation mass transport in PVDF hollow fiber membranes for ethanol–water separation, J. Membr. Sci. 362 (2010) 393-406.

[61] T. Okada, T. Matsuura, Predictability of transport equations for pervaporation on the basis of pore-flow mechanism, 70 (1992) 163-175.

[62] G. Monsalve-Bravo, S. Bhatia, Modeling Permeation through Mixed-Matrix Membranes: A Review, Processes 6 (2018) 172.

[63] M. Huš, T. Urbic, Strength of hydrogen bonds of water depends on local environment, The Journal of Chemical Physics 136 (2012) 144305.

[64] R.Y.M. Huang, C.K. Yeom, Pervaporation separation of aqueous mixtures using crosslinked poly (vinyl alcohol) (PVA), J. Membr. Sci. 51 (1990) 273-292.